Experimental

Synthesis of ZnO nanoflowers

ZnO nanoflowers were successfully obtained via hydrothermal synthesis using $ZnCl_2$ (>95%, Merck) and NaOH (98.4%, Baker Analyzed) as precursor agents. First, 0.05 M of $ZnCl_2$ was dissolved in 30 mL of deionized water, followed by the addition of NaOH until reaching pH 14, under constant magnetic stirring. Subsequently, a $Zn(OH)_2$ precipitate was formed, faciliting the removal of NaCl through multiple washing steps; the reaction is described in Equation 1. After removing the residue, the $Zn(OH)_2$ suspension was transferred into a Teflon-lined vessel and immediately sealed within a stainless-steel autoclave. The autoclave was then placed in a muffle furnace (Yamato, model FO200CR) for 2 h at 200 ºC. Finally, the resulting product was dried at 90 ºC (Equation 2) for further analysis.

$$ZnCl_2 + 2NaOH \rightarrow Zn(OH)_2 + \downarrow 2Na^+ + 2Cl^- \quad (1)$$

$$Zn(OH)_2 \rightarrow ZnO + H_2O \quad (2)$$

Preparation of Ag/ZnO nanocomposites

Ag nanoparticles were deposited onto ZnO nanoflowers (previously obtained via hidrothermal synthesis) using a photochemical deposition technique. Equimolar solutions of $AgNO_3$ and $NaNO_3$ (0.01, 0.05, 0.1 and 0.2 M) were prepared in 30 mL of deionized water and stirred briefly. Subsequently, the nanostructured ZnO powder was added and the mixture was kept under dark conditions and irradiated with a 254 nm UV lamp for 30 min under stirring. The product was washed to remove residual species and dried in a muffle furnace at 60 ºC for 6 h prior to characterization.

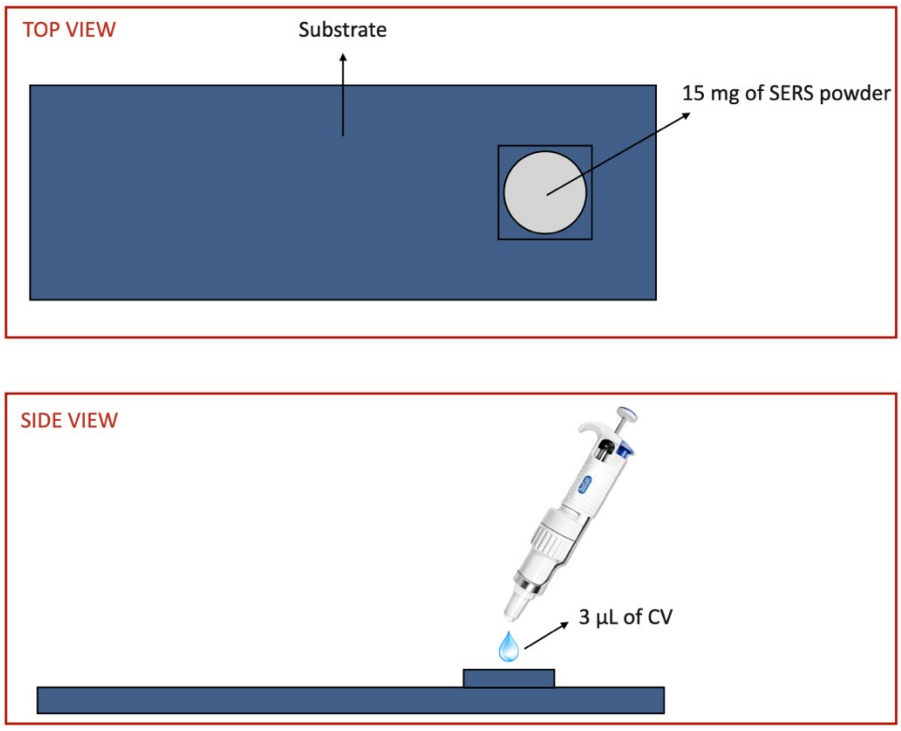

Fig. S1. CV loading onto SERS substrate.

Characterization

SEM images were recorded using a JEOL JSM-7600F field-emission scanning electron microscope (FESEM). TEM images and STEM–EDS elemental mapping were obtained with a JEOL JEM-ARM 200F microscope. XRD patterns were collected on a Bruker D8 Advance diffractometer (λ = 1.5406 Å).

Results & discussion

Morphology of ZnO nanostructures

ZnO nanoflowers were successfully synthesized, as confirmed by the SEM and TEM images shown in **Fig. S2**. Low-magnification observations reveal a high degree of uniformity and homogeneity (**Fig. S2a**). The nanostructures exhibit a flower-like morphology composed of ultrathin two-dimensional ZnO nanosheetes with thicknesses below ~20 nm (**Fig. S2b,c**). Randomly distributed pores smaller than ~10 nm are also observed (**Fig. S2d**), confirming the porous nature of the nanosheets forming the nanoflowers.

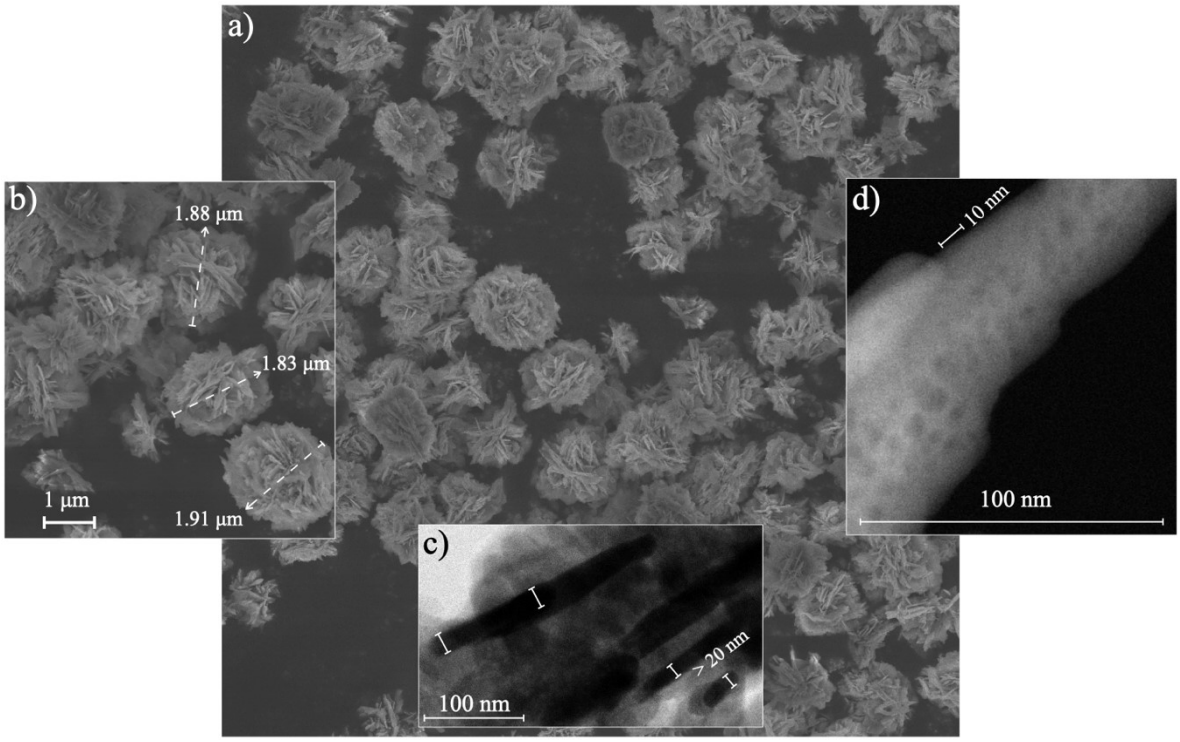

Fig. S2. SEM (a, b) and TEM (c, d) images of ZnO nanoflowers (composed of nanosheets) synthesized by hydrothermal route. Sections a, b, c and d show the uniformity of the structural uniformity, the flower size, nanosheet thickness and pore size of the nanosheets, respectively.

EDS and XRD results of Ag/ZnO nanocomposites

Fig. S3 shows the EDS spectra along with the corresponding elemental composition data of Ag/ZnO nanocomposites synthesized at different equimolar $AgNO_3$:$NaNO_3$ precursor concentrations. The results reveal a proportional increase in the Ag content deposited on the ZnO surface as the precursor concentration increases. These findings demonstrate that the deposition method allows precise control of Ag loading, enabling the fabrication of Ag/ZnO nanocomposites with tunable Ag content.

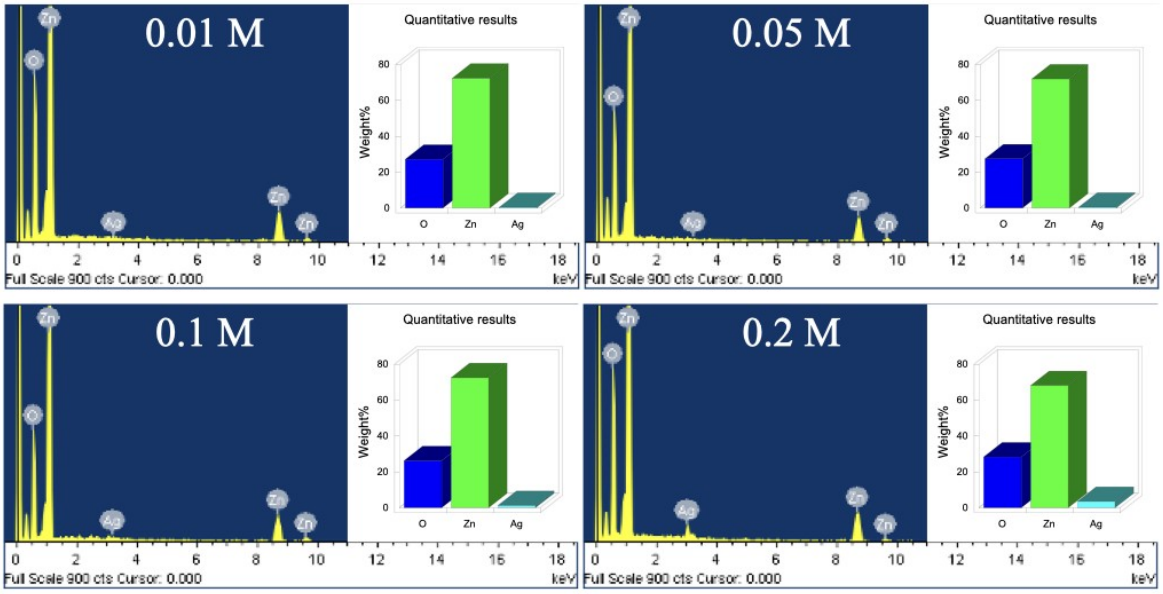

Fig. S3. EDS spectra and elemental composition data of Ag/ZnO nanostructures obtained at different $AgNO_3$:$NaNO_3$ concentrations (from 0.01 to 0.2 M).

Fig. S4 presents the X-ray diffraction (XRD) patterns of pure ZnO and Ag/ZnO nanocomposites containing different Ag loadings (0.14, 0.17, 0.43, and 1.17 at.%). All diffraction peaks can be unequivocally indexed to the hexagonal wurtzite structure of ZnO, in good agreement with the reference card CSD No. 2300112. No additional reflections associated with secondary phases or impurities were detected, indicating the high phase purity of the synthesized materials. Notably, no characteristic diffraction peaks corresponding to metallic Ag were observed in any of the Ag/ZnO samples. This behavior can be attributed to the relatively low Ag content, which is below the detection limit of conventional XRD for a segregated crystalline phase. In addition, the Ag species are likely highly dispersed over the ZnO surface, producing weak and broadened diffraction signals that overlap with the ZnO background.

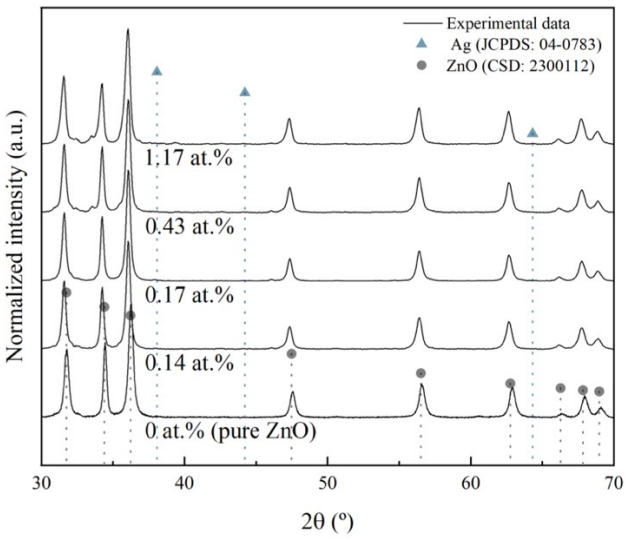

Fig. S4. XRD patterns of ZnO nanoflowers and Ag/ZnO nanostructures at different Ag loading (from 0.14 to 1.17 at.%).

CV detection

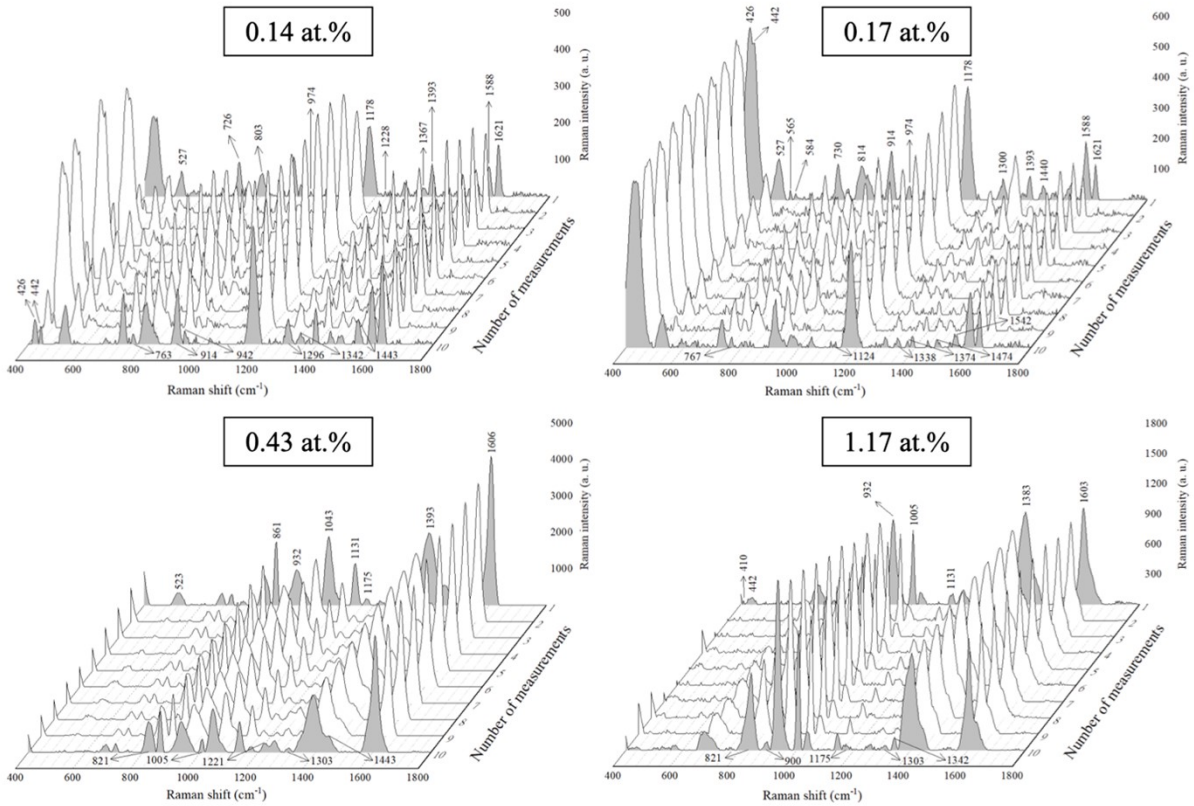

Fig. S5. Detection of CV (10^{-5} M) employing SERS substrates at different Ag content: from 0.14 to 1.17 at.%.

Table SI. Observed Raman peaks in CV and their assignments.			
Assignments	**Raman shift (cm^{-1})**		**Ref**
	Other works	**Our samples**	
Bending mode of C-C_{center}-C	333, 336, 339, 340	335	[1], [2], [3], [4], [5]
Out-of-plane bending mode of C-C_{center}-C	410, 416	410	[6], [7]
Bending mode of C-N-C	420, 422, 424, 425, 426	426	[1], [2], [7],[3] , [4], [5]
Bending mode of C-C ring	440, 441, 442, 443, 450	442	[1], [2], [3], [8], [5]
Bending mode of C-N-C	518, 521, 522, 526	519, 523, 527	[9], [6], [2], [7], [3], [4], [5]
Out-of-plane aromatic C-C deformation	557, 558, 560, 561, 562	565	[9], [6], [2], [10], [11], [4], [8], [5]
Ring skeletal vibration of radical orientation	563, 578	584	[12], [13]
Bending mode of C-N-C	607, 608	611	[2], [8]
Stretching mode of C-C_{center}-C	629	633	[8]
C-N-C symmetric stretching vibration	720, 722, 723, 725, 726, 729, 732	726, 730, 737	[9], [6], [14], [2], [7], [3], [10], [11], [4], [8], [5]
C-C_{center}-C symmetric stretching	759, 761, 769	763, 767, 770	[2], [8], [5]
Out-of-plane C-H bend	796, 797, 798, 799, 800, 801, 804	803	[9], [14], [2], [7], [3], [15], [10], [11], [4], [8], [13]
Bending mode of C-H ring	808, 817	814, 821	[1], [12]
C-H out-of-plane bending modes	908, 913, 915, 916	900, 914	[9], [6], [2], [7], [3], [10], [11], [4], [5]
Stretching of C-C ring	941, 943	932, 942	[1], [2], [5]
Ring skeletal vibration of radical orientation	954	960	[12]
Bending of $(CCC)_{breathing}$	970	974	[8]
Bending of CCC ring	983	981	[5]
Ring skeletal vibration of radical orientation	1006, 1008	1005	[7], [12]
Stretching of C-N	1123, 1126	1124, 1131	[8], [5]
C-H in-plane bending mode	1169, 1171, 1172, 1173, 1174, 1178, 1179, 1180, 1185	1175, 1178	[9], [1], [6], [2], [7], [3], [15], [10], [11], [4], [8], [5], [12], [13]
C-H in-plane aromatic mode	1186, 1193	1188	[14]
C-H rocking	1220, 1222	1221, 1228	[3], [8]
Ring C-C stretching	1291, 1297, 1298, 1299, 1300, 1302, 1305	1296, 1300, 1303	[9], [2], [3], [15], [10], [11], [16], [4], [8], [5], [12], [13]
C-C_{center}-C symmetric stretching	1328, 1336	1338	[8]
C-H in-plane bending mode	1348, 1352	1342	[14], [4]
Stretching vibration of nitrogen and phenyl ring	1357, 1364, 1368, 1371, 1374, 1377	1367, 1374	[6], [14], [2], [3], [10], [11], [12]
Stretching vibration of nitrogen and phenyl ring	1381, 1383, 1389, 1390, 1392, 1394, 1397	1383, 1393	[9], [6], [2], [7], [3], [4], [12], [13]
Bending of CH	1419	1415	[8]
CCC asymmetric stretching	1442, 1444, 1446, 1447, 1448	1440, 1443	[2], [3], [10], [11], [8], [5], [12]
CH_3 asymmetric stretching	1474, 1475	1474, 1480	[2], [8], [5]
Bending mode of C_{ring}-N	1532, 1533, 1535, 1536, 1537, 1542	1539, 1542	[9], [1], [2], [3], [10], [11], [16], [4], [5]
In-plane aromatic C-C	1579, 1583, 1584, 1585	1585, 1588	[6], [7], [10], [11], [4]
Out-of-phase ring C-C stretching	1587 and 1622, 1588 and 1618, 1590 and 1609, 1614, 1616, 1617, 1618, 1620, 1621	1603, 1606, 1621	[9], [6], [14], [2], [7], [3], [10], [11], [4], [13]

References

[1] W. Meng, F. Hu, L.-Y. Zhang, X.-H. Jiang, L.-D. Lu, and X. Wang, "SERS and DFT study of crystal violet," *J Mol Struct*, vol. 1035, pp. 326–331, Mar. 2013, doi: 10.1016/j.molstruc.2012.10.066.

[2] R. Chadha, N. Maiti, and S. Kapoor, "Triplet and SERS study of crystal violet in presence of metal nanoparticles," *Chem Phys Lett*, vol. 579, pp. 68–72, Jul. 2013, doi: 10.1016/j.cplett.2013.05.069.

[3] X. Chen, T. H. D. Nguyen, L. Gu, and M. Lin, "Use of Standing Gold Nanorods for Detection of Malachite Green and Crystal Violet in Fish by SERS," *J Food Sci*, vol. 82, no. 7, pp. 1640–1646, Jul. 2017, doi: 10.1111/1750-3841.13766.

[4] R. M. Liu, Y. P. Kang, X. F. Zi, M. J. Feng, M. Cheng, and M. Z. Si, "The ultratrace detection of crystal violet using surface enhanced Raman scattering on colloidal Ag nanoparticles prepared by electrolysis," *Chinese Chemical Letters*, vol. 20, no. 6, pp. 711–715, Jun. 2009, doi: 10.1016/j.cclet.2009.02.001.

[5] B. Wang, L. Zhang, and X. Zhou, "Synthesis of silver nanocubes as a SERS substrate for the determination of pesticide paraoxon and thiram," *Spectrochim Acta A Mol Biomol Spectrosc*, vol. 121, pp. 63–69, Mar. 2014, doi: 10.1016/j.saa.2013.10.013.

[6] K. Lai, Y. Zhang, R. Du, F. Zhai, B. A. Rasco, and Y. Huang, "Determination of chloramphenicol and crystal violet with surface enhanced Raman spectroscopy," *Sens Instrum Food Qual Saf*, vol. 5, no. 1, pp. 19–24, Mar. 2011, doi: 10.1007/s11694-011-9106-8.

[7] K. Zhang, T. Zeng, X. Tan, W. Wu, Y. Tang, and H. Zhang, "A facile surface-enhanced Raman scattering (SERS) detection of rhodamine 6G and crystal violet using Au nanoparticle substrates," *Appl Surf Sci*, vol. 347, pp. 569–573, Aug. 2015, doi: 10.1016/j.apsusc.2015.04.152.

[8] L. Li and W. S. Chin, "Rapid Fabrication of a Flexible and Transparent Ag Nanocubes@PDMS Film as a SERS Substrate with High Performance," *ACS Appl Mater Interfaces*, vol. 12, no. 33, pp. 37538–37548, Aug. 2020, doi: 10.1021/acsami.0c07178.

[9] T. N. Q. Trang, L. To Cam Huong, T. Duong, and V. Thi Hanh Thu, "Ag-grafted on ZnO nanorod arrays using UV-assisted irradiation for enhanced SERS behavior in CV detection," *Science and Technology Development Journal*, vol. 24, no. 2, p. first, May 2021, doi: 10.32508/stdj.v24i2.2519.

[10] D. Xu, Y. Zhang, S. Zhang, W. Yang, and J. Chen, "Ultrasensitive SERS detection of crystal violet and malachite green based on high surface roughness copper nanocorns prepared via solid-state ionics method," *Sens Actuators A Phys*, vol. 331, p. 113042, Nov. 2021, doi: 10.1016/j.sna.2021.113042.

[11] D. Xu, Y. Zhang, S. Zhang, W. Yang, Z. Wang, and J. Li, "Copper nanoleaves SERS substrates with high surface roughness for sensitive detection crystal violet and rhodamine 6G," *Opt Laser Technol*, vol. 145, p. 107502, Jan. 2022, doi: 10.1016/j.optlastec.2021.107502.

[12] E. J. Liang, X. L. Ye, and W. Kiefer, "Surface-Enhanced Raman Spectroscopy of Crystal Violet in the Presence of Halide and Halate Ions with Near-Infrared Wavelength Excitation," *J Phys Chem A*, vol. 101, no. 40, pp. 7330–7335, Oct. 1997, doi: 10.1021/jp971960j.

[13] M. Vinod and K. G. Gopchandran, "Au, Ag and Au:Ag colloidal nanoparticles synthesized by pulsed laser ablation as SERS substrates," *Progress in Natural Science: Materials International*, vol. 24, no. 6, pp. 569–578, Dec. 2014, doi: 10.1016/j.pnsc.2014.10.003.

[14] M. Volný, A. Sengupta, C. B. Wilson, B. D. Swanson, E. J. Davis, and F. Tureček, “Surface-Enhanced Raman Spectroscopy of Soft-Landed Polyatomic Ions and Molecules,” *Anal Chem*, vol. 79, no. 12, pp. 4543–4551, Jun. 2007, doi: 10.1021/ac070278a.

[15] G. Yang *et al.*, “Fabrication of paper-based SERS substrates by spraying silver and gold nanoparticles for SERS determination of malachite green, methylene blue, and crystal violet in fish,” *Microchimica Acta*, vol. 187, no. 5, p. 310, May 2020, doi: 10.1007/s00604-020-04262-2.

[16] W. Wei and Q. Huang, “Preparation of cellophane-based substrate and its SERS performance on the detection of CV and acetamiprid,” *Spectrochim Acta A Mol Biomol Spectrosc*, vol. 193, pp. 8–13, Mar. 2018, doi: 10.1016/j.saa.2017.11.062.